Indian Journal of Pure & Applied Physics
Vol. 56, October 2018, pp. 765-772

Determination of structural elements of synthesized silver nano-hexagon from X-ray diffraction analysis

Sumit Sarkar & Ratan Das*

Nano-Physics & Nanotechnology Research Laboratory, Department of Physics, Tripura University, Suryamaninagar 799 022, India

Received 13 November 2017; accepted 5 April 2018

Silver nano-hexagons (AgNHs) have been prepared by a chemical reduction method using poly-vinyl pyrrolidone (PVP) as a stabilizing agent. The XRD results exhibit the crystalline nature of the prepared sample, with a face centred cubic (fcc) phase. Transmission electron microscopic (TEM) results reveal that the silver nanoparticles are nearly hexagon in shape with an average size of 50 nm. Here, crystallite size has been calculated using Williamson-Hall (W-H) method, which is nearly matching with average size obtained from TEM analysis. Again, using W-H method, micro strain has been calculated, which is produced in the nano-hexagon due to dislocation of silver atoms. Further, the lattice constant of the nano-hexagons has also been estimated from the Nelson–Riley plot. Moreover, the appropriate structural parameters such as Lorentz factor, Lorentz polarization factor, dislocation density, number of atoms in a unit cell and morphological index have also been studied from the X-ray diffraction profile.

Keywords: Silver nano-hexagon, Lorentz factor, Lattice constant, Dislocation density, W-H analysis

1 Introduction

Nanostructure materials are attracting the world of science due to their unusual properties[1-3]. Like all other properties, elastic properties also changes, when the size of the material approaches the nano-scale. Many properties like mechanical properties, structural properties, phase identification etc. can be obtained from X-ray profile analysis. In general, X-ray related techniques are superior to other characterization method to understand the structural properties in inorganic nanomaterials. X-ray profile analysis is a simple and powerful tool to estimate the crystallite size and lattice strain in nanomaterials[4]. But, the pseudo-Voigt function and Warren–Averbach (W–A) analysis method, mainly based on Fourier co-efficients of the XRD line profile, are very critical method to obtain the crystallite size, lattice strain[5-8]. However, Williamson–Hall (W–H) analysis for the diffraction peak profile is relatively a simple and good method over the pseudo-Voigt function and Warren–Averbach (W–A) analysis method. For this reason, we have used here this W-H analysis for the study of the particle size and intrinsic strain only. In general, the particle size (D) can be calculated using the Scherrer equation[9]:

$$D = k\lambda/\beta \cos\theta \quad \text{.... (1)}$$

Where k, is called Scherrer constant[10,11], λ is the wavelength of the incident X-rays (0.1541 nm), β is the full-width at half-maximum (FWHM) of the peak (in radians) and θ is the Bragg angle. As the total broadening of the X-ray diffraction peak is due to the sample and the instrument, the β-parameter needs to be corrected in the Scherrer equation. For this correction, a standard silicon sample with small micro strain and large particle size is generally used so that the diffraction peak widths are due to the instrumental broadening only. Let β_{expt} be the measured width, β_{stand} be the width due to standard sample, i.e., the instrumental width, and β the corrected one, then the expression for the instrumental effect correction[12] as:

$$\beta = (\beta^2_{expt} - \beta^2_{stand})^{1/2} \quad \text{... (2)}$$

Clearly, this size broadening is independent of the reflection order, that is, independent of the diffraction angle[12]. This measure of the domain size generally gives a volume-weighted quantity[12-15]. In this method, Scherrer neglects the importance of the micro strain (ε), where as, its effects remain presents in the diffraction pattern, as this intrinsic strain also produce the broadening in the X-ray profile[13,14]. The contribution of the micro strain to the line broadening of the diffraction peak is defined by Stokes and Wilson[13] as:

*Corresponding author (E-mail: dasratanphy@gmail.com, dasratantuphy@tripurauniv.in)

$$\beta_\varepsilon = 4\varepsilon \tan\theta \quad \ldots (3)$$

Based on the work of Stokes and Wilson-Hall[15], a method has been proposed for separating the crystallite size and micro strain contributions to the line broadening analysis, which depends on their reflection order. The method came to be known as Williamson-Hall (W-H) method. Williamson-Hall plotting is the one of the best and simple method to separate the particle size and micro strain in the line broadening analysis of the X-ray diffraction pattern[4,15,16]. Further, this method is based on the approximation that the line profile due to particle size (D) and micro strain (ε) broadening is Lorentzian and the total broadening is given by:

$$\beta = \beta_D + \beta_\varepsilon \quad \ldots (4)$$

Where, β is considered the sum of the width due to the micro strain β_ε and due to particle size β_D. By Williamson–Hall (W-H) method, the separation of these size and strain effects are possible as:

$$\beta_{hkl} \cos\theta = (k\lambda/D) + 4\varepsilon \sin\theta \quad \ldots (5)$$

W-H plotting consists of a plot of $\beta_{hkl} \cos\theta$ versus $\sin\theta$, which becomes a straight line, when the sample exhibits homogeneous distribution of particle size and micro strain. The slope provides the micro strain, whereas the mean particle size can be obtained from the intercept. The slope of the plot may be positive, negative or horizontal, which reflects the cause of the strain. The positive slope indicates a lattice expansion, whereas the negative slope indicates a lattice compression but the horizontal slope indicates about a crystal free from any micro strain.

In this present work, we have calculated the average particle sizes for silver nano-hexagon using the Williamson-Hall plotting method, considering the effect of micro-strain, in addition to the crystalline size effect and correcting the instrumental broadening using the silicon as the standard sample. This result is comparable to the average sizes obtained from TEM study. Further, using the XRD profile, we have calculated other structural parameters for the prepared silver nano-hexagon sample, such as dislocation density, lattice constant etc., where the data obtained from the W-H plot has been used for determining these parameter. The most important part of X-ray profile is that, the intensity of the diffraction peaks is not same for different angles. The reason behind this is the presence of an important factor, what is called Lorentz -polarization factor. In this present work, we have determined this factor and also analysed how this factor regulates the intensity of different peaks corresponding to the different angles.

2 Experimental

2.1 Nano-hexagon preparation

Many studies have exhibited that the morphology and the crystal structure of the nanoparticles strongly depend on the reaction conditions like temperature, precursor concentration, and molar ratio[17,18]. In this process, ethylene glycol (EG) served as both reductant and solvent, and poly- vinyl pyrrolidone (PVP) served as the capping reagent and stabilizer. For the preparation of silver nano-hexagons, PVP (0.28 M based on the repeating unit, M_w = 10,000) have been dissolved in 15 mL of EG and $AgNO_3$ (0.18 M) solution also have been dissolved in 15 mL of EG. The two solutions are immediately subjected into magnetic stirrers with room temperature. The $AgNO_3$/EG solution gradually turn brown color during stirring around 30 min, indicating that some Ag nanoparticles have been formed. The PVP/EG solution remains clear and colourless[3,19]. A flask containing 15 mL of EG is heated also with vigorous stirring nearly 140 °C. Both of these two solutions $AgNO_3$/EG and PVP/EG are simultaneously injected slow drop-wise into the hot EG by a two channel syringe. During the injection process the temperature decreases to 120 °C. After the completion of injection process the temperature remains fixed at 160 °C for 6 h. After cooling to room temperature, the silver nano-hexagon sample has been characterized for further study.

2.2 TEM image analysis

Transmission electron microscopy (TEM) is used for the study of the morphology, size distribution, and crystalline direction of the nano-materials. Here, morphological studies of the prepared silver nano-hexagons have been performed on a TEM Model: JEM-2100 instrument with an accelerating voltage of 200 kV. TEM image of the prepared PVP capped silver nano-hexagon is shown in Fig. 1, which shows that the prepared silver nano-hexagons have almost uniform size distribution with an average size of 50 nm.

2.3 X-ray diffraction (XRD) analysis

The X-ray diffraction profile actually can provide much information about the crystals in a material. Size obtained from TEM analysis is not actually the average effect of the sample but provide the information from a very narrow region of a particular

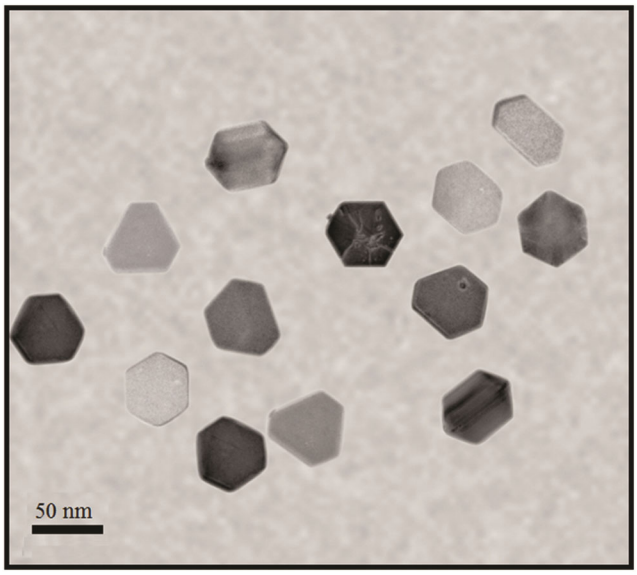

Fig. 1 — TEM micrograph of the prepared silver nano-hexagons.

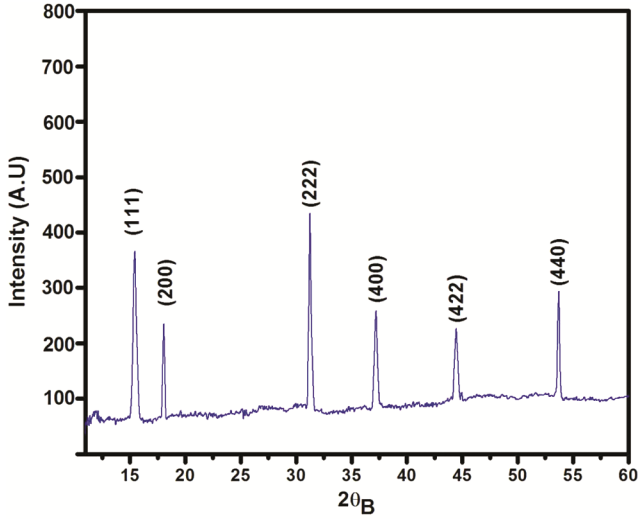

Fig. 2 — X-ray diffraction pattern of silver nano-hexagon sample.

mesh of the TEM grid but XRD profile analysis can rectify this drawbacks and provide information about the whole sample[20-24]. The X-ray diffraction experiments were performed in a Rigaku powder diffractometer (DMAXB) using the Bragg–Brentano geometry in a continuous mode with a scan speed of 0.25°/min. A CuKα radiation tube with the line focus was operated at 40 kV and 25 mA. The X-ray powder diffractions were taken in the range of 20–90° (2Θ) in step sizes of 0.05°. The diffracted X-ray beam coming from the sample is focused into the detector slit with a curved graphite monochromator. The X-ray diffraction pattern of the prepared silver nano-hexagon sample is shown in Fig. 2. A number of strong Bragg reflections can be seen in the profile, which correspond to the (111), (200), (222) (400), (422) and (440) reflections of fcc silver. All of these reflections correspond to pure silver metal with face centered cubic (fcc) symmetry. The high intense peak for fcc materials is generally (111) or (222) reflection, which is observed in this sample. The intensity profile in this X-ray diffraction pattern shows the good crystallinity of the prepared silver nano-hexagons.

3 Results and Discussion

3.1 Lorentz polarization factor

Peak intensities in the X-ray profile are not same for different planes and for different angles as well. It is found that there are a number of factors that further show θ dependence of the peak intensities. In the first place, diffraction generally occurs for angles slightly different from the value predicted by Bragg's Law, where the intensity[25], $I \propto 1/\sin(2\theta)$. Second factor is that, on satisfying Bragg's Law, orientation of the number of crystals is highest for low angles and for which we get, $I \propto \cos(\theta)$[25]. Further, it has been observed[25] that the fraction of the diffraction cone that intersects the detector is highest at low angles and for which, $I \propto 1/\sin(2\theta)$. On combining all these factor and after doing trigonometric manipulation, we obtain the Lorentz Factor as $I \propto 1/(4\sin^2\theta \cos\theta)$. This Lorentz factor provides the reason for the differing times spent by the different reflections in the diffraction condition[26].

On rotating the crystal in a beam of monochromatic X-ray radiation, different planes of the crystal gets rotated, where they satisfy the condition for reflection. X-ray radiation in each reflection depends on the time taken to reflect[26]. The Lorentz factor is actually this time factor and hence the Lorentz factor is directly proportional to the time taken in each reflection. So it is inversely proportional to the velocity with which the different plane passes through the condition of reflection[26,27]. The individual velocity of each reflection can be understood from the viewpoint of reciprocal lattice. The reciprocal lattice points take different times to traverse the Ewald sphere[28]. Many reciprocal lattice points cross the Ewald sphere with a path normal to the sphere surface and those which are far from the rotation axis having trajectories with maximum velocities, must pass quickly through the Ewald sphere[29]. But reciprocal lattice points with trajectories having small grazing angles relative to the sphere surface and smaller velocities will pass slowly, as these are closer to the rotation axis[29,30]. All these reasons produce the Lorentz factor, $1/(4\sin^2\theta \cos\theta)$.

Table 1 — Morphology index, particle size, Lorentz factor and Lorentz polarization factor of silver nano-hexagon sample for different planes.

Planes	2θ (Degree)	FWHM	Particle size (nm)	Lorentz factor	Lorentz polarization factor	Morphological index (MI)
(111)	15.50	0.0030	50	14.175	109.473	0.606
(200)	18.03	0.0038	41	10.309	78.521	0.539
(222)	31.24	0.0040	39	3.579	24.789	0.518
(400)	37.18	0.0038	41	2.591	16.935	0.549
(422)	44.47	0.0044	38	1.886	11.386	0.513
(440)	53.68	0.0047	37	1.372	7.407	0.500

Again, an X-ray along the *x*-axis has electric vector oscillates in a direction perpendicular to the *x*-axis. The *y*-component and *z* component of the X-ray will get scattered in a different way, as the angle between the scattered beam and the electric field gradient are different[31,32]. On resolving the original unpolarised incident X-ray beam into two plane polarised components, the total scattered intensity is obtained as the sum of the intensities of these two components, which depends on the scattering angle[33] (2θ). This gives rise to the polarization factor[33], where $I \propto (1+\cos^2 2\theta)/2$.

Combined these Lorentz and polarization terms, to get the Lorentz-polarization (LP) factor and we find that $I \propto (1+\cos^2 2\theta)/(8\sin 2\theta \cos\theta)$. Lorentz factor is actually combined with the polarization factor for the X-ray intensity calculations. This Lorentz-polarization factor plays an important role in controlling the X-ray intensity with respect to the diffraction angle[34-43] and hence its evaluation is very essential for different analysis, where it depends on the intensities of diffraction maxima, such as in the analysis of one-dimensional crystal structure. Due to this Lorentz factor, the intensity of the reflection peaks decreases for intermediate angles but for the smaller or higher angles, intensities are higher as compared to the intermediate angles. This means that intensities are always higher for the forward or backward directions. This Lorentz factor and Lorentz Polarization factor are calculated from the following equations[41,42], which are given in the Table 1:

$$\text{Lorentz Factor} = (1/4 \sin^2\theta \cos\theta) \quad \ldots (6)$$

$$\text{Lorentz polarization factor} = (1 + \cos^2 2\theta)/(\sin^2\theta \cos\theta) \quad \ldots (7)$$

As it is clear from the expression that the Lorentz-polarization factor strongly varies with the Bragg angle θ, the intensity of reflections at intermediate Bragg angles is decreased compared to those at high or low angles.

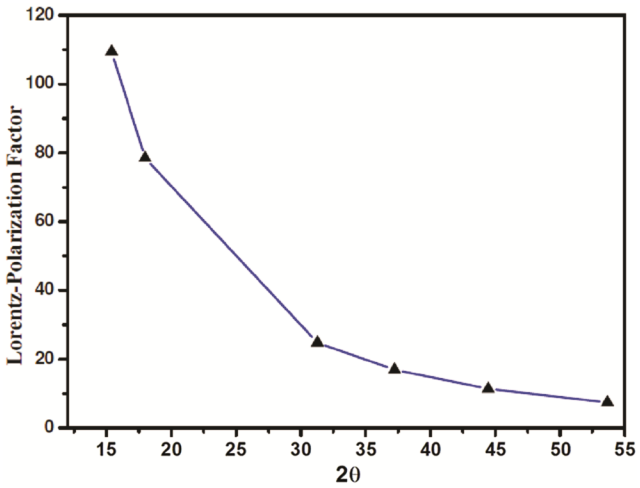

Fig. 3 — The Lorentz-polarization factor as a function of 2θ.

Figure 3 shows a graph of the Lorentz-polarization factor for the X-ray diffraction pattern. Here it has been observed that the Lorentz-polarization factor is very large at low angles and then it reaches a minimum around 60°. For this one reasons that low-angle peaks are of greater intensity than high angle peaks in X-ray diffraction pattern. So, X-ray diffraction pattern of the as prepared nanoparticles showing the intensity profile, which is as per the Lorentz-polarization factor.

3.2 Williamson-Hall analysis

Williamson–Hall analysis is generally used for the study of the average size calculation and intrinsic micro strain that gets generated in the nanoparticles. Here the FWHM has been obtained after correcting the instrumental broadening, considering the Si as the standard sample. The average particle size and the micro strain have been calculated using the Williamson-Hall plotting according to the Eq. (5), which is shown in Fig. 4. The good straight line in the Williamson-Hall plotting indicates no dispersion in the particle size and micro strain, suggesting that the sample has homogeneous particle size distribution and micro strain.

The crystallite size and micro strain can be estimated from the intercept of the *y*-axis and the slope of the line, respectively. The size and micro strain of silver nano-hexagons are found to be 48 nm and 2.30×10^{-3}, respectively. The quantity, correlation coefficient measures the strength and the direction of a linear relationship between two variables. A correlation coefficient of greater than 0.8 is generally described as strong, whereas a correlation less than 0.5 is generally described as weak correlation. Here, we have obtained a correlation coefficient of 0.88, showing a good linear relationship between these two variables. Further, the approximate results of Williamson-Hall analysis are capable of giving a qualitative indication of sample microstructure. Many authors[11,22] reported that the positive signal of the micro-strain indicates a lattice expansion. Our results of positive micro-strain, indicate a lattice expansion in the prepared silver nano-hexagon.

3.3 Nelson-Riley plot analysis

In a crystal, different imperfections namely stacking faults, dislocation arrays, as well as twins produce the size broadening. But different major defect such as vacancies, interstitials and mainly dislocations, creates the strain in the sample. As the dislocation density[8,23] depends on the lattice constant, so lattice constants have to be determined for the determination of dislocation density. Nelson-Riley plot is very useful method for the lattice constant determination. For cubic crystals, we have the equation:

$$1/d^2 = (h^2+k^2+l^2)/a^2 \quad \ldots (8)$$

Where d is the inter-planar spacing determined by using Bragg's equation, a is the lattice constant and hkl are the Miller planes of the crystal. The Nelson-Riley plot is a graph of the calculated values of lattice constant for different planes versus the error function $F(\theta)$ which is given by[23]:

$$F(\theta) = [(\cos^2\theta/\sin\theta) + (\cos^2\theta/\theta)]/2 \quad \ldots (9)$$

The lattice constant can be obtained from the intercept of the Nelson- Riley plot. The general procedure to obtain the apparent lattice constant a by plotting these values against some function of the Bragg angle θ, and to extrapolate to a value[44] corresponding to θ = 90°. Further, the linearity of the plot at very high angles should provide an accurate value of the lattice constant [44]. The error function satisfies this criterion. Moreover, this error function has a great significance on determining the lattice constant as the error function becomes minimum when $F(\theta) = 90°$, which

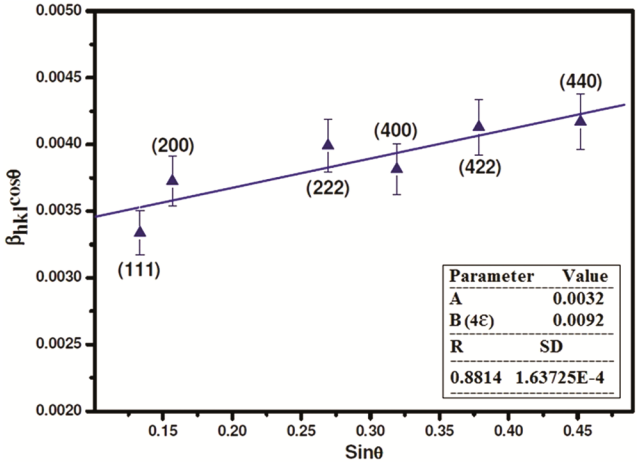

Fig. 4 — Williamson–Hall plot for silver nano-hexagon sample.

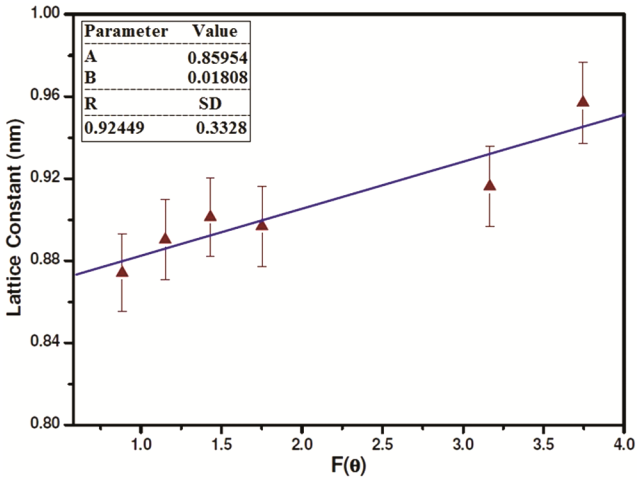

Fig. 5 — Nelson–Riley plot for silver nano-hexagon sample.

corresponds to the extreme back-reflection along the path of the incident beam. This error function arises out of three different types of systematic error such as absorption of the X-ray beam in the sample, the shifting of the rotation axis of the sample relative to the geometric centre, called as the eccentricity error, and finally, inaccurate determination of the camera constants[44]. For extrapolation of the graph corresponding to θ = 90°, low-angle limit of linearity of the plot should be as low as possible as it gives a consistent value for a and the compression of the high-angle points towards the extrapolation limit should be considerable[44]. Further, the slope of the extrapolation should be as small as possible. In our plot, more number of points has been obtained towards that is, towards $F(\theta) \rightarrow 0$ giving a value of the lattice constants with greater accuracy.

A typical Nelson–Riley plot for a silver nano-hexagon sample is shown in Fig. 5, where the corrected value of lattice constant (a) is obtained by

extrapolating the plot. The lattice parameter as obtained from Nelson-Riley plot is found to be 0.8595 nm and this value estimated from this plot is almost free from systematic errors. This value of lattice constant is signifying the fact that a lattice expansion takes place due to intrinsic strain as produced in the silver nano-hexagon, which has already been confirmed from the W-H plot. This calculated value of lattice constant is further used below to calculate the dislocation density of silver nano-hexagon.

3.4 Estimation of dislocation density

The deviation of the lattice constant of the as-prepared silver nano-hexagon sample from the bulk value indicates the presence of strain in this sample. This deviation is related to the change in atomic positions in the nanocrystals from their perfect order. Further, this rearrangement of atoms in the prepared nanocrystals produces a broadening of the diffraction peaks[23]. Hence, a lattice distortion takes place due to this dislocation of atoms. So, dislocations are lattice defects in crystalline materials, which get increased when the crystal size is reduced to the nanometer scale[45].

It has been shown that the dislocation density, i.e., dislocation lines per unit volume of the crystal increases, while the grain size decreases with increasing strain and ultimately these parameters reach saturation values[46-52]. The dislocation density in the sample has been determined using this equation[8,49-50]:

$$\beta_{hkl} \cos\theta = (4a\delta/15)D \quad \ldots (10)$$

where a is the lattice constant (in nm) estimated from the Nelson–Riley plot and D is the particle size (in nm) calculated from Scherrer formula. β_{hkl} cosθ has been plotted along the y-axis and D along the x-axis, which is shown in Fig. 6.

Dislocation density has been estimated from the slope of the fitted line. The dislocation density of silver nano-hexagons is found to be 4.136×10^{14} m^{-2} with the correlation coefficients value 0.99725.

3.5 Morphology index

It is well known that silver nanoparticles have been widely used in many diverse industries due to their unique structural, physical and chemical properties, which are reflected by its hardness, surface properties, particle size and morphology. Morphology index (MI) is an important parameter which gives a linear relationship[41] with the particle size. The respective size has been calculated using Debye Scherrer formula for each diffraction planes, considering their

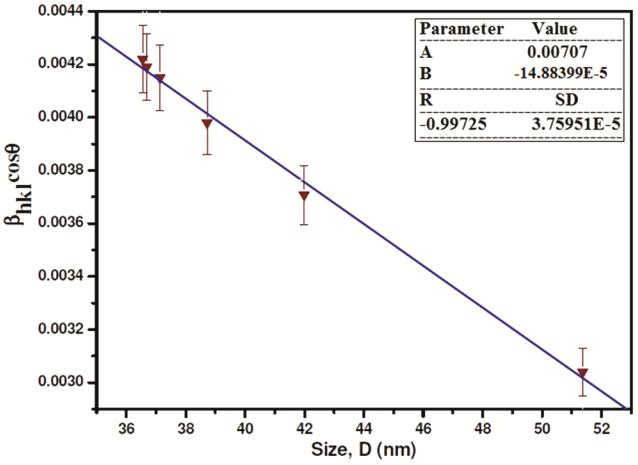

Fig. 6 — $\beta_{hkl}\cos\theta$ versus size (D) for silver nano-hexagon sample.

respective FWHM. Here, Morphology index (MI) has been calculated from FWHM of XRD data using the relation:

$$MI = FWHM_h / (FWHM_h + FWHM_p) \quad \ldots (11)$$

Where $FWHM_h$ is highest FWHM value obtained from XRD peaks and $FWHM_p$ is value of particular peak's FWHM for which MI is to be calculated. The relation between morphology index (MI) and particle size is shown in Table 1.

The range of morphological index for experimental silver nano-hexagon sample is found to be lie between 0.50 to 0.60 and the details are presented in Table 1. From the plot of size versus MI as shown in the Fig. 7, it is observed that MI is correlated with the particle size, where particle size ranges from 37 to 50 nm. Further, it is also observed that morphological index is directly proportional to particle size with a small deviation having a linear fit. The observed results of the M.I confirm the uniformity and fineness of the prepared nano-hexagons.

4 Conclusions

In this paper, we have reported the analysis of XRD profile of synthesized silver nano-hexagons for the determination of different structural parameters. The size calculated from XRD is found to be 48 nm sizes, which matches with the results obtained from TEM image. Further, we have shown that how does the Lorentz-polarization factor (LPF) regulates the intensity of XRD profile and this result also explain the XRD profile of silver nano-hexagon. Finally, we have determined the lattice constant with nearly zero error from the Nelson-Riley plot and is found to be around 0.8595 nm, which further has been used to

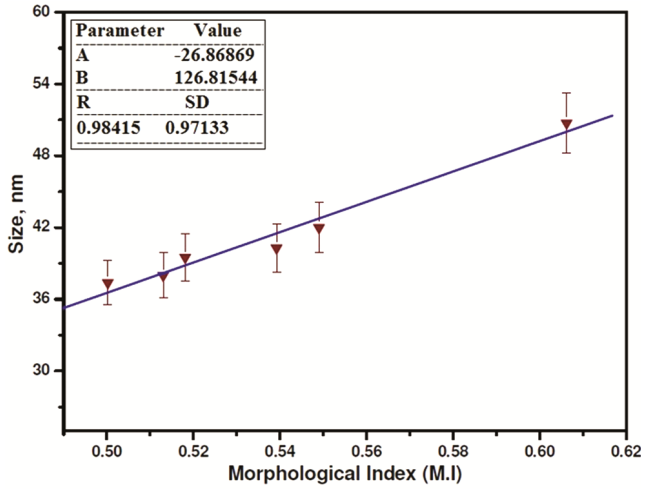

Fig. 7 — Morphological Index (MI) versus particle size (*D*) of silver nano-hexagon.

calculate the dislocation density and is found as 4.136×10^{14} m^{-2}. At last, we have shown that the M.I gives a linear relationship with size of the silver nano-hexagon.

Acknowledgement

We are thankful to the SAIF, North Eastern Hilly University, Shillong, India for conducting the TEM analysis and to Department of Physics, Manipur University, Manipur, India, for providing the X-ray diffraction data for silver nano-hexagon.

References

1 Das R & Sarkar S, *Opt Mater*, 48 (2015) 203.
2 Rao C N R & Biswas K, *Ann Rev Anal Chem*, 2 (2009) 435.
3 Sarkar S & Das R, *Plasmonics*, 11 (2016) 551.
4 Das R & Sarkar S, *Mater Chem Phys*, 167 (2015) 97.
5 Santra K, Chatterjee P & Gupta S P, *Bull Mater Sci*, 25 (2002) 251.
6 Saravanan M S, Sivaprasad K, Susila P & Kumaresh S P, *Physica B*, 406 (2011) 165.
7 Lalena J N & Cleary D A, *Principles of inorganic materials design*, (John Wiley: New Jersey), 26 (2010) 404.
8 Das R & Sarkar S, *Curr Sci*, 109 (2015) 775.
9 Azaroff L V & Buerger M J, *Powder method in X-ray crystallography*, (McGraw-Hill Book Company: USA), 1958.
10 James R W, *The optical principles of the diffraction of X-rays*, (G Bell and Sons Ltd: London, 1962.
11 Gonçalves N S, Carvalho J A, Lima Z M & Sasaki J M, *Mater Lett*, 72 (2012) 36.
12 Cullity B D, *Elements of X-ray diffraction*, 2nd Edn, (Addison-Wesley Publishing Company), 1978.
13 Stokes A R & Wilson A J C, *Proc Phys Soc*, 56 (1944) 174.
14 Langford J L, Delhez R, de Keijser Th H & Mittemeijer E J, *Aust J Phys*, 41 (1988) 113.
15 Hall W H, *Proc Phys Soc Lond A*, 62 (1949) 741.
16 Williamson G K & Hall W H, *Acta Metal*, 1 (1958) 22.
17 Kan C X, Zhu J J & Zhu X G, *J Phys D: Appl Phys*, 41 (2008) 155304.
18 Sun Y & Xia Y, *Science,* 298 (2002) 2176.
19 Liu X, Huang R & Zhu J, *Chem Mater*, 20 (2008) 192.
20 Guinier A, *X-ray diffraction in crystals, imperfect crystals and amorphous bodies*, (Dover: New York), 1994.
21 Pinna N, *Prog Colloid Polym Sci*, 130 (2005) 29.
22 Maia A O G, Meneses C T, Menezes A S, Flores W H, Melo D M A & Sasaki J M, *J Non-Cryst Solids*, 352 (2006) 3729.
23 Gubicza J, *X-ray line profile analysis in materials science*, IGI Global, (2014) 49.
24 Hankare P P, Delekar S D, Bhuse V M, Garadkar K M, Sabane S D & Gavali L V, *Mater Chem Phys*, 82 (2003) 505.
25 Sher F, *Crystal structure determination I,* Proceedings of the National Workshop on Crystal Structure Determination Using Powder XRD, Pakistan Institute of Engineering and Applied Sciences, Khwarzimic Science Society, 2007.
26 Buerger M J & Klein G E, *J Appl Phys* 16, (1945) 408.
27 Buerger M J, *Proc Natl Acad Sci*, 25 (1939) 383.
28 Kolb U, Shankland K, Meshi L, Avilov A & David W I F, *Uniting electron crystallography and powder diffraction*, (Springer: Netherlands), 2012.
29 Thomas C H, *Diffraction: Principles and application*, EPJ Web of Conference, 104 (2015) 01002.
30 Huxley H E & Faruqi A R, *Annual Review Biophys Bioeng*, 12 (1983) 381.
31 Gnedin Y N & Silant'ev N A, *Astrophys Space Phys Reviews*, 10 (1997) 1.
32 Smorenburg P W, Kanters J H M, Lassise A, Brussaard G J H, Kamp L P J & Luiten O J, Polarization-dependent ponderomotive gradient force in a standing wave, Proc SPIE 8079, Laser Acceleration of Electrons, Protons, and Ions; and Medical Applications of Laser-Generated Secondary Sources of Radiation and Particles, 80790Z (May 25, 2011).
33 Suryanarayana C & Norton M G, *X-ray diffraction: A practical approach*, (Springer: US), 1998.
34 Compton A H & Allison S K, *X-rays in theory and experiment*, (D Van Nostrand Company, Inc: New York), 1935.
35 Clark G L, *Applied X-rays*, 4th Edn, (McGrawHill Book Company, Inc: New York), 1955.
36 Peiser H S, Rooksby H P & Wilson A J C, *X-ray diffraction by polycrystalline materials*, (The Institute of Physics: London), 1955.
37 Holtona J M & Frankel K A, *Acta Cryst D*, 66 (2010) 393.
38 Bhaumik A, Shearin A M, Delong R, Wanekaya A & Ghosh K, *J Phys Chem C*, 118 (2014) 18631.
39 May S J, Kim J-W, Rondinelli J M, Karapetrova E, Spaldin N A, Bhattacharya A & Ryan P J, *Phys Rev B*, 82 (2010) 014110.
40 Yang H, Hazen R M, Finger L W, Prewitt C T & Downs R T, *Phys Chem Minerals*, 25 (1997) 39.
41 Prabhu Y T, Rao K V, Kumari B S & Sai Kumar V S, *Adv Nanoparticles*, 2 (2013) 45.
42 Reynolds R C, *Clays Clay Minerals*, 34 (1986) 359.
43 Müller U, *Inorganic structural chemistry*, Second Edition, (John Wiley & Sons: US), 2007.
44 Nelson J B & Riley D P, *Proc Phys Soc*, 57 (1944) 160.

45 Benenson W, Harris J W, Stöcker H & Lutz H, *Handbook of physics*, (Springer-Verlag: New York), 2002.
46 Chinh N Q, Gubicza J & Langdon T G, *J Mater Sci*, 42 (2007) 1594.
47 Venkata Subbaiah Y P, Prathap P & Ramakrishna Reddy K T, *Appl Surf Sci*, 253 (2006) 2409.
48 Venkateswarlu K, Sreekanth D, Sandhyarani M, Muthupandi V, Bose A C & Rameshbabu N, *Int J BiosciBiochem Bioinform*, 2 (2012) 389.
49 Prabhu Y T, Rao K V, Kumari B S, Sai Kumar V S & Pavani T, *Int Nano Lett*, 5 (2015) 85.
50 Khan Mohd A M, Kumar S, Ahamed M, Alrokayan S A & AlSalhi M S, *Nanoscale Res Lett*, 6 (2011) 434.
51 Jacob R, Nair H G & Isac J, *Int Lett Chem Phys Astron*, 41 (2015) 100.
52 Spasojevic´ J, Radosavljevic´ A, Krstic´ J, Mitric´ M, Popovic´ M, Rakoc˘ evic´ Z, Kalagasidis Krusic M & Kac˘ arevic´ -Popovic´ Z, *Polym Compos*, 38 (2017) 1014.